Supporting Information

Single-layer carbon-coated FeCo alloy nanoparticles embedded in single-walled carbon nanotubes for high oxygen electrocatalysis

Dengyu Xie, Yu Chen, Deshuang Yu, Silin Han, Junnan Song, Yaoyi Xie, Feng Hu, Linlin Li and Shengjie Peng*

Jiangsu Key Laboratory of Materials and Technology for Energy Conversion, College of Materials Science and Technology, Nanjing University of Aeronautics and Astronautics, Nanjing 210016, P. R. China.

Experimental Section

Materials preparation

All of the reagents and chemicals utilized in the experiments were used without further purification. The commercial single-walled carbon nanotubes were produced from Nanjing XFNANO Materials Tech Co., Ltd. The carbon black was purchased from Hefei Kejing Material Tech Co., Ltd.

Synthesis of FeCo/SWCNT

Single-layer carbon-coated FeCo alloy nanoparticles encapsulated in single-walled carbon nanotubes are denoted as FeCo/SWCNT. The equipment mainly includes an electric furnace, an input device, a quartz tube as a reaction container (D=35 cm, L=1100 cm), and a collector. In this aerosol-assisted floating catalyst chemical vapor deposition method (CCVD) technique, all the reactions in the reactor happened in the gas phase. A mist of ferrocene ($(C_5H_5)_2Fe$) and cobaltocene ($(C_5H_5)_2Co$) was used as the catalysts (10 g L^{-1}), thiophene (C_4H_4S 0.3 wt.%) as an additive and argon (20 °C S^{-1}) as a protecting gas and carrier gas. Then the feedstock solution was introduced into the furnace with hydrogen (H_2) and entered into the reaction zone with the argon (Ar) flow. After heating to 800 °C, methane (CH_4) gas was introduced (50 mL min^{-1}) and reacted for 30 minutes. At the high temperature of 1150 °C, the ferrocene and cobaltocene could decompose to form bimetallic FeCo nanoparticles. Finally, the product was collected using stainless steel mesh (400 mesh) located at the cool zone in the down-stream direction of the quartz tube.

Materials characterization

Scanning electron microscopy (SEM) analysis was performed with a Regulus 8100 scanning electron microscope. High-resolution transmission electron microscopy (HRTEM) analysis was performed with an FEI Tecnai G2 F20 microscope. Phase and crystal structure were identified by a Bruker D8 Advance X-ray diffraction system with Cu-Kα radiation. Raman spectra acquired on a confocal laser micro-Raman spectrometer (Renishaw in Via) with the exciting wavelength of 514.5 nm. The X-ray photoelectron spectroscopy (XPS) test was carried out on a Thermo ESCALAB 250 system to investigate the chemical states of the materials. Brunauer-Emmett-Teller (BET) method and the Barrett-Joyner-Halenda (BJH) method were applied to calculate the specific surface areas and pore size distributions, respectively.

Electrochemical measurements

OER test

The electrochemical performance was conducted in a three-electrode electrochemical cell by using the Autolab electrochemical workstation. The Ag/AgCl electrode, platinum foil, and nickel foam were respectively applied as the reference, counter, and the working electrodes with a 1.0 M KOH electrolyte. The catalyst ink was prepared by mixing the catalyst (1 mg), PVDF dispersion (0.05 mL, 1 mg PVDF dissolved in 50 μl NMP), and ethanol (2.95 mL). Drop casting was employed to fabricate the electrodes wherein the slurry was deposited onto 1 × 2 cm^2 nickel foam (loading amount is approximately ~0.1 mg cm^{-2}). While the RuO_2 slurry was prepared by mixing 7 mg catalyst, 2 mg Super P, and 50 μl PVDF dispersion (the loading mass is approximately ~1.0 mg cm^{-2}). Linear sweep voltammetry was conducted at a scan rate of 0.1 mV s^{-1} with the polarization measurements being iR-corrected. Reversible hydrogen electrodes (RHE) were used to calibrate the reference electrode. The cyclic voltammetry (CV) method was then employed to evaluate the double-layer capacitance (C_{dl}). The voltage window of cyclic voltammograms was 1.07-1.17 V *vs* RHE. Meanwhile, the electrochemical surface area (ECSA) was estimated by using C_{dl}. The ECSA can be calculated by the following equation: ECSA ≈ C_{dl} /C_s, where C_s is the specific capacitance of the electrocatalyst under an identical electrolyte condition[1-3].

ORR test

The test was conducted in a three-electrode electrochemical cell by using the Autolab electrochemical workstation. The rotating disk electrode (RDE) test was used at a

sweep rate of 5 mV s^{-1}. Namely, glassy carbon electrode (d = 0.5 cm, S = 0.196 cm^{-2}), KCl-saturated Ag/AgCl and Pt wire as the working, reference and counter electrodes with 0.1 M KOH as the electrolyte, respectively. The catalyst ink was prepared by adding 5 mg electrocatalyst into 950 μl ethanol, and 50 μl Nafion (5 wt.%). After ultrasonic treatment for more than 2 hours, 20 μl of the ink was placed on a 0.196 cm^2 glassy carbon for the test (0.510 mg cm^{-2}). For contrast, Pt/C (20 wt.%) catalyst ink was also obtained in a similar way (0.510 mg cm^{-2}). Reversible hydrogen electrodes (RHE) were used to calibrate the reference electrode.

Assembly of aqueous Zn-air batteries

The Zn-air battery was constructed by zinc plate anode, 6.0 M KOH electrolyte with 0.2 M $ZnCl_2$ dissolved and air catalysts coated on carbon cloth with a loading of 1.0 mg cm^{-2} as the cathode. Pt/C + RuO_2 mixed electrode was prepared with a mass ratio of 1:1. The performance for the batteries was tested by Neware testing devices without the flowing of oxygen.

Assembly of flexible solid Zn-air batteries

The structure of the flexible solid Zn-air battery contains zinc plate anode, solid electrolyte, and FeCo/SWCNT coated on 1×2 cm^2 carbon cloth cathode. Polyacrylic acid (PAA) KOH was used as a solid electrolyte. The synthesis procedure of PAA KOH is as follows. Firstly, 0.01 g Methylene-Bis-Acrylamide (MBAA) was dissolved into 2.2 mL polyacrylic acid, and ultrasound for 10 minutes. Then add 10 mL 8.4 M KOH into the above PAA solution with continuous stirring. Finally, 80 μl 0.15 M $K_2S_2O_8$ was further added and stirred for 30 seconds. The mixture was placed at room temperature for 4 hours to form PAA KOH gel. The area of air electrode is 1×2 cm^2 with the average catalyst loading of 1.0 mg cm^{-2}.

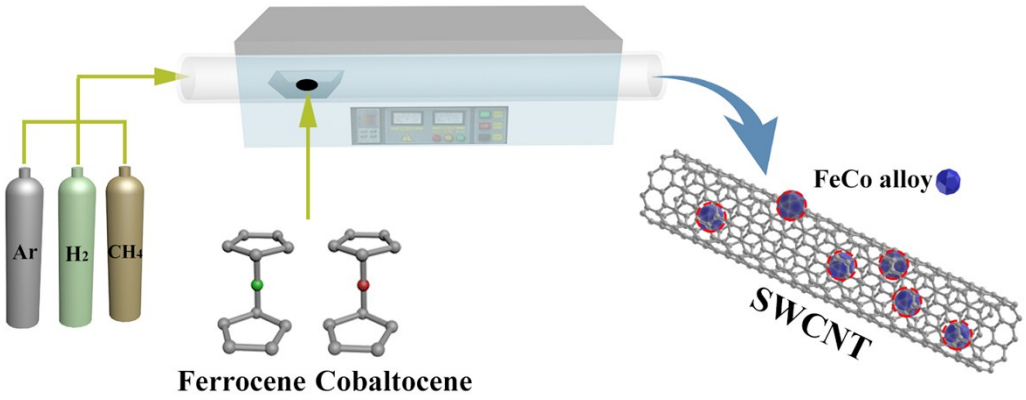

Scheme S1 A scheme of the synthesis reactor used for the growth of FeCo/SWCNT.

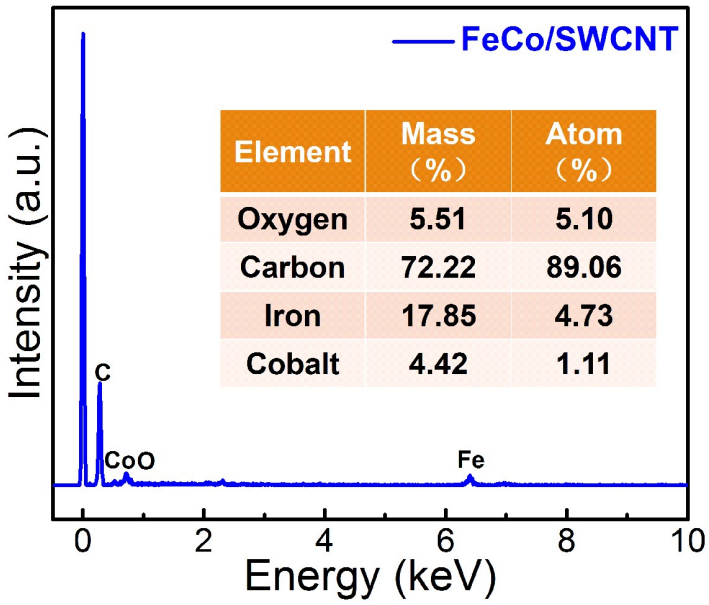

Fig. S1 EDS elemental analysis of FeCo/SWCNT with the inset showing the relative contents of Fe, Co, O, and C in it.

(a)

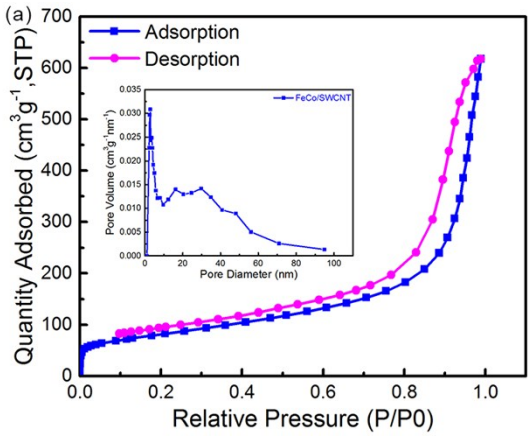

(b)

Samples	BET Surface Area (m^2 g^{-1})
FeCo/SWCNT	282.63
Commercial SWCNT	380.00
Carbon black	62.00

Fig. S2 a) N_2 adsorption/desorption isotherms with the inset pore size spectrum of FeCo/SWCNT. b) BET surface area of FeCo/SWCNT, commercial SWCNT, and carbon black.

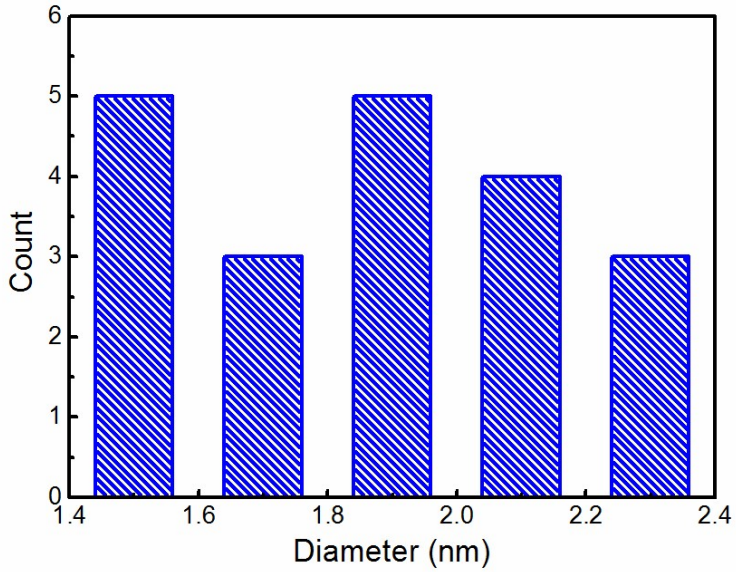

Fig. S3 Diameter distribution of SWCNTs in FeCo/SWCNT measured from HRTEM images.

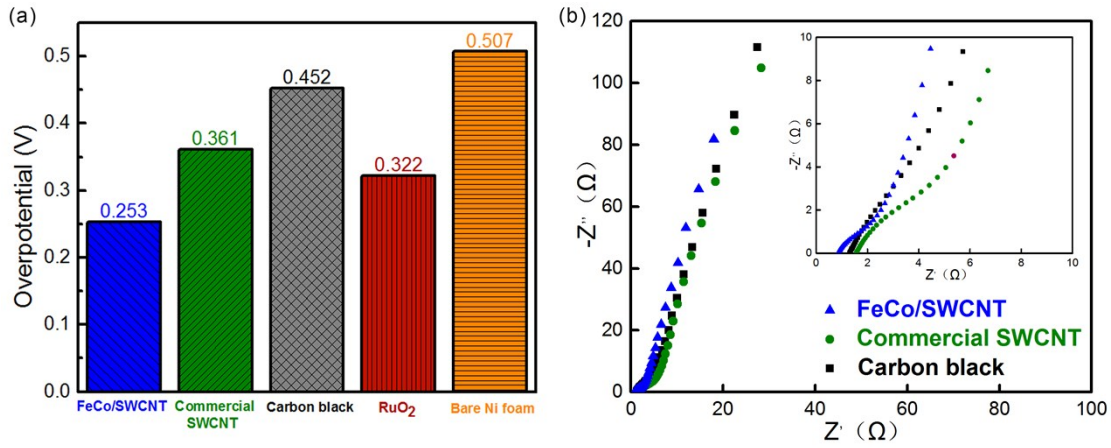

Fig. S4 a) The corresponding overpotentials at 10 mA cm^{-2} current density of FeCo/SWCNT, commercial SWCNT, carbon black, RuO_2, and bare Ni foam. b) EIS Nyquist for FeCo/SWCNT, commercial SWCNT, and carbon black.

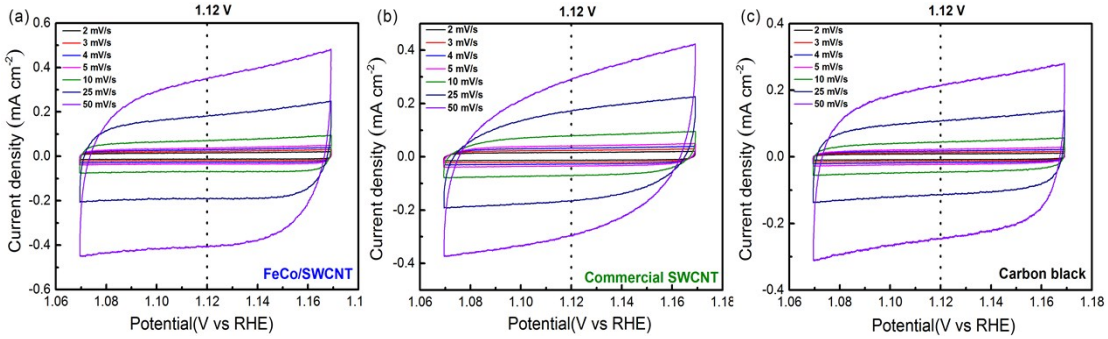

Fig. S5 CVs of a) FeCo/SWCNT, b) commercial SWCNT and c) carbon black at different scan rates from 2 to 50 mV s^{-1} in 1.0 M KOH solution.

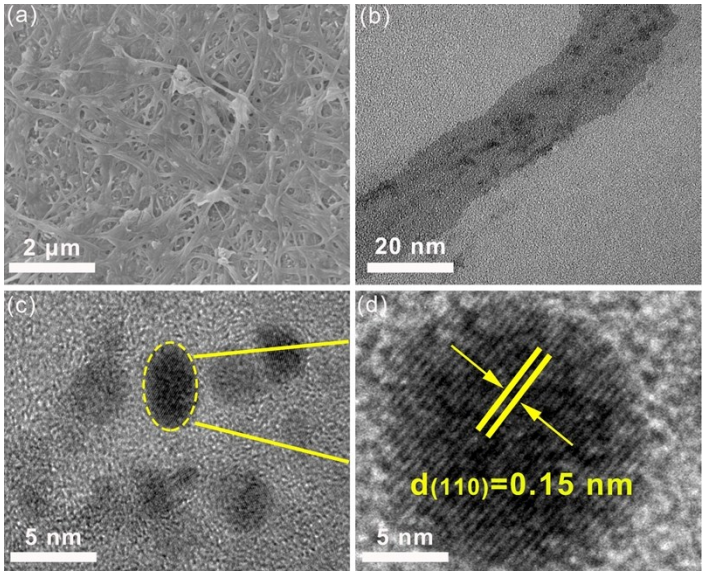

Fig. S6 a) SEM, b) TEM, and c), d) HRTEM images of FeCo/SWCNT after long-term OER electrolysis.

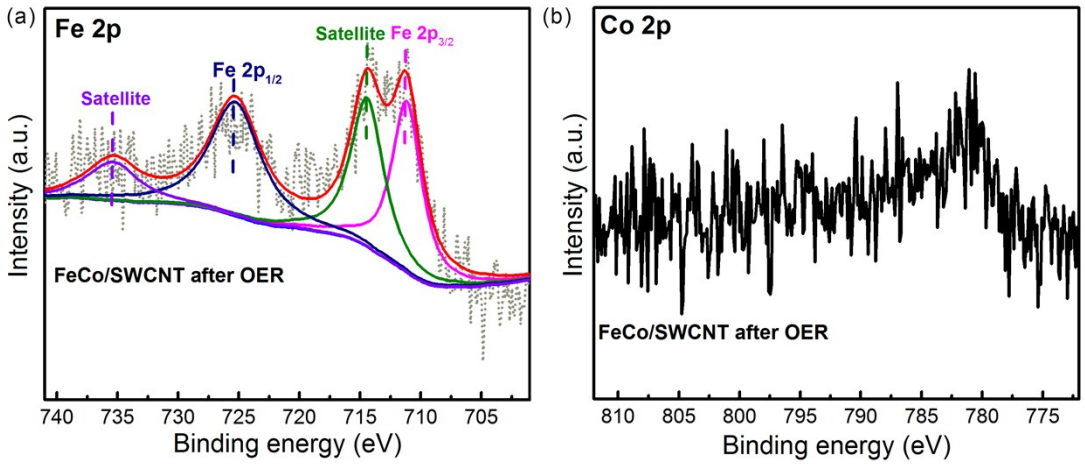

Fig. S7 a) Fe 2p and b) Co 2p XPS images of FeCo/SWCNT after long-term OER electrolysis.

Fig. S7 distinctly shows that the original peaks representing the zero-valence state of Fe and Co disappeared. While ionic state peaks and shakeup satellites of Fe 2p and Co 2p are detected to shift to higher binding energy regions in comparison to those in pristine FeCo/SWCNT. The scrambled diffraction peaks of Co 2p may be due to its relatively less content in FeCo/SWCNT and partially oxidized on the surface under the OER chronopotentiometry test.

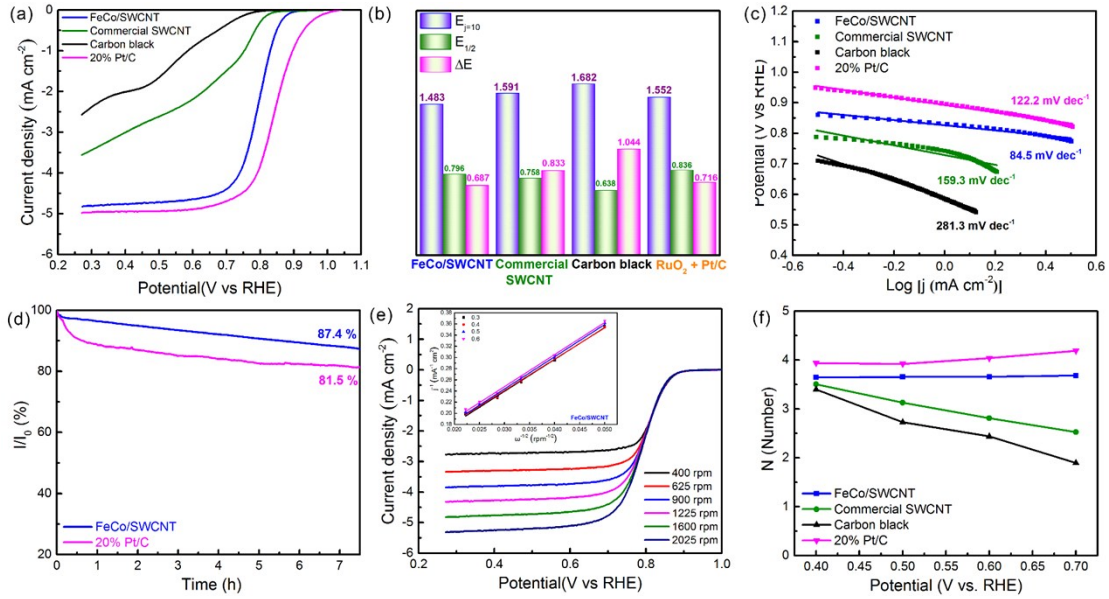

Fig. S8 a) LSV curves at the speed of 1600 rpm in O_2 atmosphere, b) The overpotentials $E_{j=10}$ of OER, the half-wave potentials $E_{1/2}$ of ORR and ΔE ($E_{j=10} - E_{1/2}$) between OER and ORR for FeCo/SWCNT, commercial SWCNT, carbon black and RuO_2 + Pt/C. c) Tafel plots of FeCo/SWCNT, commercial SWCNT, carbon black, and 20% Pt/C respectively. d) Chronoperometric responds of FeCo/SWCNT and 20% Pt/C. e) Polarization curves of FeCo/SWCNT at the rotating speed from 400 to 2025 rpm with inset showing the responding K-L plots and f) Electron transfer number (n) calculated from the K-L equation at the different potential of FeCo/SWCNT, commercial SWCNT, carbon black and 20% Pt/C.

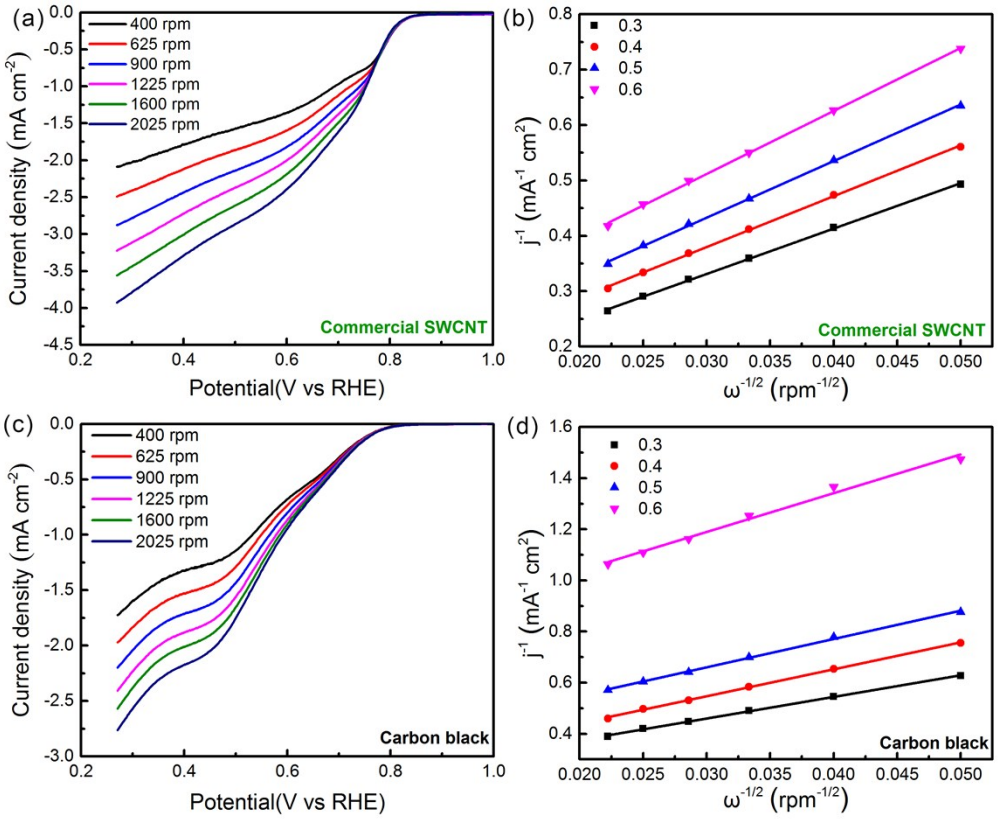

Fig. S9 a), c) Polarization curves of commercial SWCNT and carbon black at the rotating speed from 400 to 2025 rpm. b), d) responding K-L plots of commercial SWCNT and carbon black.

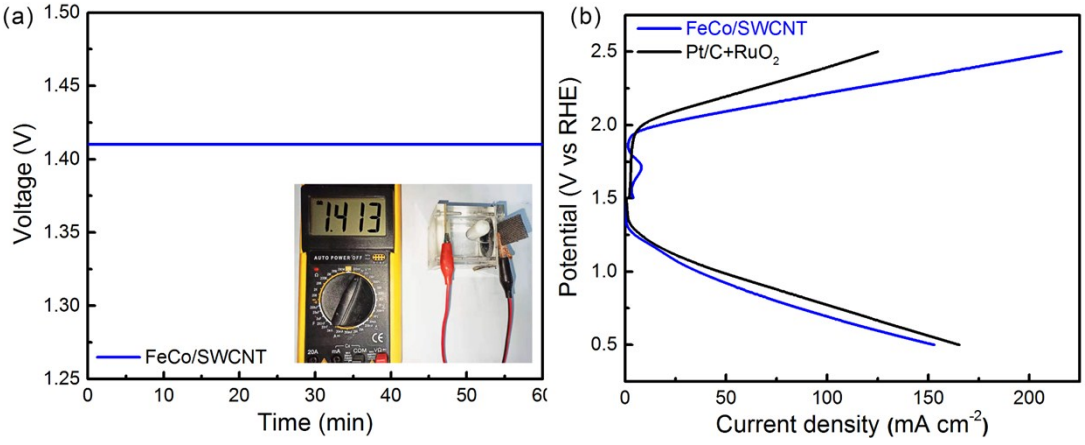

Fig. S10 Aqueous rechargeable Zn-air batteries performance with FeCo/SWCNT and Pt/C + RuO_2 acting as the air cathodes. a) Open circuit plots and b) The charging-discharging polarization curves.

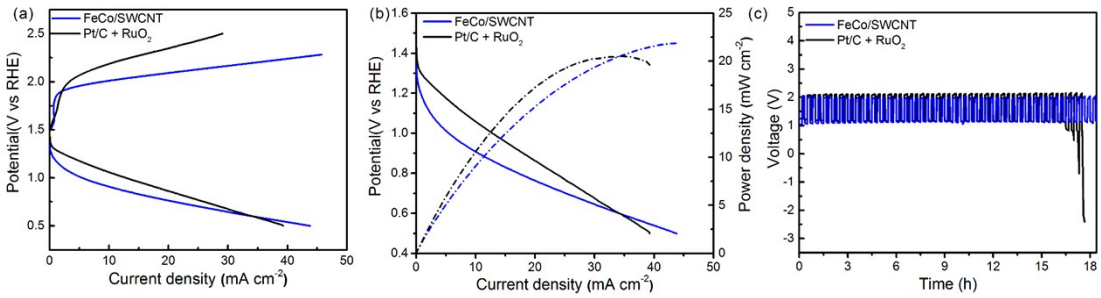

Fig. S11 All-solid-state rechargeable Zn-air batteries performance with FeCo/SWCNT and Pt/C + RuO_2 acting as the air cathodes. a) The charging-discharging polarization curves. b) Discharging polarization curves and the corresponding power density plots and c) Cycling performance at the charging and discharging current density of 1 mA cm^{-2}.

Table S1 Comparison of the OER and ORR activity of the previously reported non-precious catalysts in the KOH solution.

Samples	$E_{j=10}$ (V)	$E_{1/2}$ (V)	ΔE (V)	Reference
FeCo/SWCNT	1.48	0.80	0.68	This Project
CoNi/BCF	1.60	0.80	0.80	4
N-GCNT/FeCo-3	1.73	0.92	0.81	5
FeCo-NC_{ps}	1.61	0.85	0.76	6
FeCo@MNC	1.47	0.86	0.61	7
NPCN/ CoNi-NCNT	1.59	0.87	0.72	8
NiFe@NBCNT	1.43	0.83	0.60	9
FeCo-Co_4N/N-C	1.51	0.76	0.75	10
CoNi@NCNT/NF	1.54	0.87	0.67	11
NCNT/CoO-NiO-NiCo	1.50	0.83	0.67	12
$Ni_{50}Fe_{50}$/N-CNTs	1.55	0.86	0.69	13
FeCo/N-DNC	1.62	0.81	0.81	14
FeCo-DHO/NCNTs	1.55	0.86	0.69	15

1. M. Li, Y. Zhu, H. Wang, C. Wang, N. Pinna, and X. Lu, *Adv. Energy Mater.*, 2019, 9, 1803185.
2. X. Luo, Q. Zhou, S. Du, J. Li, J. Zhong, X. Deng, and Y. Liu, *ACS Appl. Mater. Inter.*, 2018, 10, 22291−22302.
3. Z. Lv, M. Tahir, X. Lang, G. Yuan, L. Pan, X. Zhang, and J.-J. Zou, *J. Mater. Chem. A*, 2017, 5, 20932−20937.
4. W. Wan, X. Liu, H. Li, X. Peng, D. Xi, and J. Luo, *Appl. Catal. B: Environ.*, 2019, **240**, 193−200.
5. C. Y. Su, H. Cheng, W. Li, Z. Q. Liu, N. Li, Z. Hou, F. Q. Bai, H. X. Zhang, and T. Y. Ma, *Adv. Energy Mater.*, 2017, **7,** 1−12.
6. J. Liu, T. He, Q. Wang, Z. Zhou, Y. Zhang, H. Wu, Q. Li, J. Zheng, Z. Sun, Y. Lei, J. Ma, and Y. Zhang, *J. Mater. Chem. A*, 2019, **7**, 12451−12456.
7. C. Li, M. Wu, and R. Liu, *Appl. Catal. B: Environ.*, 2019, **244**, 150−158.
8. Y. Hou, S. Cui, Z. Wen, X. Guo, X. Feng, and J. Chen, *Small*, 2015, **11**, 5940−5948.
9. D. Bin, B. Yang, C. Li, Y. Liu, X. Zhang, Y. Wang, and Y. Xia, *ACS Appl. Mater. Interf.*, 2018, **10**, 26178−26187.
10. X. Zhu, T. Jin, C. Tian, C. Lu, X. Liu, M. Zeng, X. Zhuang, S. Yang, L. He, H. Liu, and S. Dai, *Adv. Mater.*, 2017, **29,** 1704091.
11. W. Niu, S. Pakhira, K. Marcus, Z. Li, J. L. Mendoza Cortes, and Y. Yang, *Adv. Energy Mater.*, 2018, **8,** 1800480.
12. X. Liu, M. Park, M. G. Kim, S. Gupta, G. Wu, and J. Cho, *Angew. Chem. Int. Ed. Engl.*, 2015, **54**, 9654−9658.
13. Y. Chen, J. Peng, W. Duan, G. He, and Z. Tang, *ChemCatChem*, 2019, **11**, 5994−6001.
14. G. Fu, Y. Liu, Y. Chen, Y. Tang, J. B. Goodenough, and J. M. Lee, *Nanoscale*, 2018, **10**, 19937−19944.
15. M. Wu, Q. Wei, G. Zhang, J. Qiao, M. Wu, J. Zhang, Q. Gong, and S. Sun, *Adv. Energy Mater.*, 2018, **8,** 1801836.

References